Nanometer Resolution Self-Powered Static and Dynamic Motion Sensor Based on Micro-Grated Triboelectrification

Yu Sheng Zhou, Guang Zhu, Simiao Niu, Ying Liu, Peng Bai, Qingsheng Jing, and Zhong Lin Wang*

Measurement of displacement and speed at the micro- and nano-scale has ubiquitous applications in the scientific and industrial fields such as manufacturing, automation, robotics, and nano-manipulation. Traditionally well-established techniques to detect displacement or speed include optical approaches based on optical interference,[1,2] electrical techniques based on capacitive sensing,[3,4] electromagnetic induction,[5] and piezoelectric sensors.[6–8] However, there is always a trade-off among resolution, working distance and design complexity.[1–7] Furthermore, most of the existing sensing technologies need pre-provided electrical or optical signals in order to detect the mechanical displacement, which inevitably requires external power sources. However, the increased number and density of portable electronic devices and sensing networks today desperately desires low power consumption and/or self-powered sensors.[8–13]

In previous work, we showed great potential of triboelectric nanogenerators (TENG)[14–17] in mechanical energy harvesting based on triboelectrification and electrostatics, and the possibility of utilizing it for self-powered pressure or chemical sensors.[13,17,18] A recently developed segmentally structured disk TENG also shows its potential to serve as a self-powered sensor to measure the rotation speed.[19] Herein, we demonstrate a self-powered, one-dimensional displacement and speed sensing technology based on the coupling of triboelectric effect and electrostatic induction, achieving high resolution, large dynamic range and long detecting distance, which overcomes a trade-off dilemma in many existing technologies. The sensor consists of a pair of micro grating structures and relative motion between two gratings leads to periodic separation of two micro-grated dielectric materials that are oppositely charged through triboelectrification. As a result, an alternating electric signal between the metal electrodes placed beneath the dielectric materials can be detected due to electrostatic induction. The displacement and speed can be detected in real time by monitoring the open

circuit (OC) voltage and short circuit (SC) current generated by the sensor itself, respectively. With a grating pair having a period of 200 µm, the displacement resolution of 173 nm was achieved in tens of millimeters working distance with a linearity error of 0.02%. The speed can be directly detected by the amplitude of the short circuit current, which has a good linearity over a large dynamic range from 5 µm s^{-1} to 0.1 m s^{-1}. The resolution for both displacement and speed sensing can be further improved by reducing the grating period. This new approach for displacement/speed sensing distinguishes itself from the existing technologies by a combination of self-powered, nanometer resolution, long detecting range and non-optical compacted structure, showing extensive potential applications in automation, manufacturing, process control, portable device, etc.

The motion sensor consists of two micro gratings with identical patterns, as sketched in **Figure 1**a. The grating at the bottom (60 mm x 30 mm) is made of an etched silicon wafer coated with aluminum as the bottom electrode and silicon dioxide as triboelectrically positive material; the grating on the top (30 mm x 15 mm) is made of patterned SU-8 film (17 µm in thickness) on a glass slide as supporting substrate and subsequently coated with Indium tin oxide (ITO) and Parylene film as the top electrode and triboelectrically negative material, respectively (Figure 1a inset). Transparent materials are selected for the top grating to adjust the alignment between the two gratings. Figures 1c,d and Figures 1e,f show the optical pictures and detailed microscopic structure of the as-fabricated devices, respectively. In working condition, the top grating slides within the scope of the bottom grating in a direction perpendicular to the grating strips. The detailed fabrication processes are described in Experimental Section.

The operating principle is illustrated in **Figure 2**. When the two gratings are brought into contact with each other, charges transfer between the two surfaces due to contact electrification. Because Parylene is more triboelectrically negative than SiO$_2$, the Parylene surface is negatively charged and SiO$_2$ surface positively charged. A relative sliding between the two gratings separates two tribo-charged surfaces, resulting in an electrical potential between two metal electrodes through electrostatic induction, which can be detected as open circuit (OC) voltage. If the two electrodes are connected through external circuits, the built-in voltage will drive electrons flowing from one electrode to the other when a short circuit (SC) current can be detected. Finite element simulations using COMSOL show the OC voltage and the amount of SC charge induced on the top electrode as a function of positions within a cycle, as drawn in Figure 2. The parameters used in simulation are listed in Supplementary Information (Figure S1, Supporting Information). For the first half cycle when the top micro-grating moves from

Y. S. Zhou,[+] Dr. G. Zhu,[+] S. Niu,[+] Y. Liu, P. Bai,
Q. Jing, Prof. Z. L. Wang
School of Materials Science and Engineering
Georgia Institute of Technology
Atlanta, Georgia, 30332–0245, United States
E-mail: zlwang@gatech.edu
Prof. Z. L. Wang
Beijing Institute of Nanoenergy and Nanosystems
Chinese Academy of Sciences
Beijing, China

[+]Y. S. Z., G. Z. and S. N. contributed equally to this work.
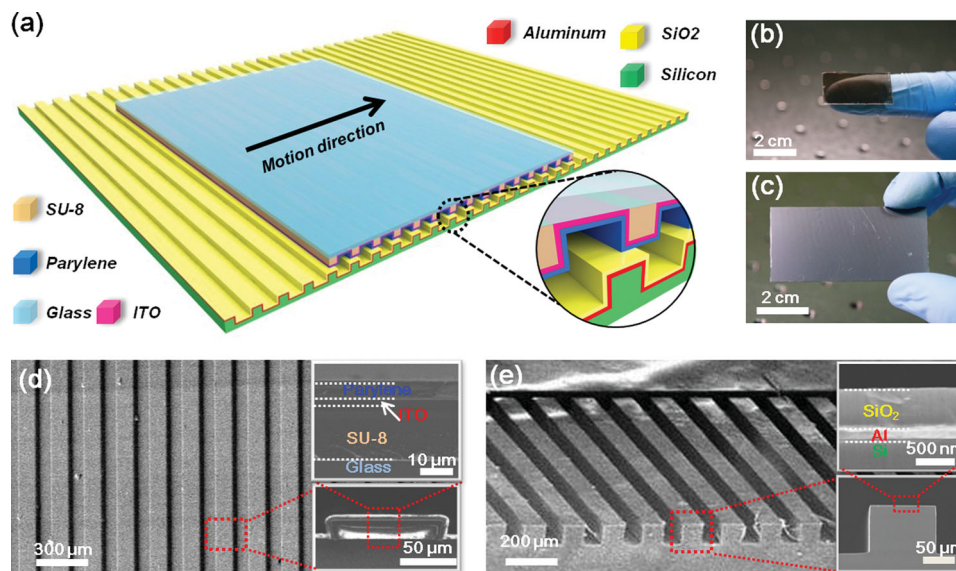
Figure 1. Structure of a triboelectric motion sensor. (a) Schematic of a pair of micrograting and detailed information of layers illustrated in the inset. (b,c) Optical photograph of as-fabricated micrograting pair with sizes of ~30 × 15 mm² for the top grating and ~60 × 30 mm² for the bottom grating. (d) Scanning electron microscopic (SEM) images of the top micrograting with glass slide substrate. The insets show the cross section: the ITO layer on top of the patterned SU-8 photoresist serves as the top electrode, and the outmost layer is Parylene film serving as electronegative material that participates in the triboelectric charge transfer. (e) SEM images of the bottom micrograting. The insets show the cross section profile: the etched Silicon is coated with Al as bottom electrode and SiO₂ as electropositive material for triboelectrification.

overlap to separation position, the OC voltage and the amount of induced charge increases from zero to their maximums, and accordingly the SC current is positive; for the second half cycle when the top micro-grating moves from separation to overlap position, the OC voltage and the amount of induced charge decreases from their maximums to zero, and accordingly the SC current changes to be negative.

Continuous movement alternates the two oppositely charged surfaces between overlap and separation, thus generating an alternating OC voltage or SC current output. Therefore, by counting the number (*n*) of the voltage peaks and valleys (or the current zero-crossings), the displacement can be calculated to be *nP*/2, where *P* is the period of the grating. Benefited from the fact that the output signal originates from about 150 pitches that are in parallel, the sensor has large tolerance of variations caused by non-uniform surface charge distribution, surface contamination or grating defects.

To characterize the motion sensor, a uniform speed (1mm s⁻¹) motion test was carried out. Detailed description of the experiment setup is shown in Methods and Supporting Information (Figure S2). During the movement, the OC voltage measured between the two electrodes (**Figure 3**a) alternates between 0 and ~160 mV periodically, and the frequency is about 5 Hz (Figure 3b). As aforementioned, since each cycle corresponds to one period of the gratings, which is 200 µm in this device, the real time
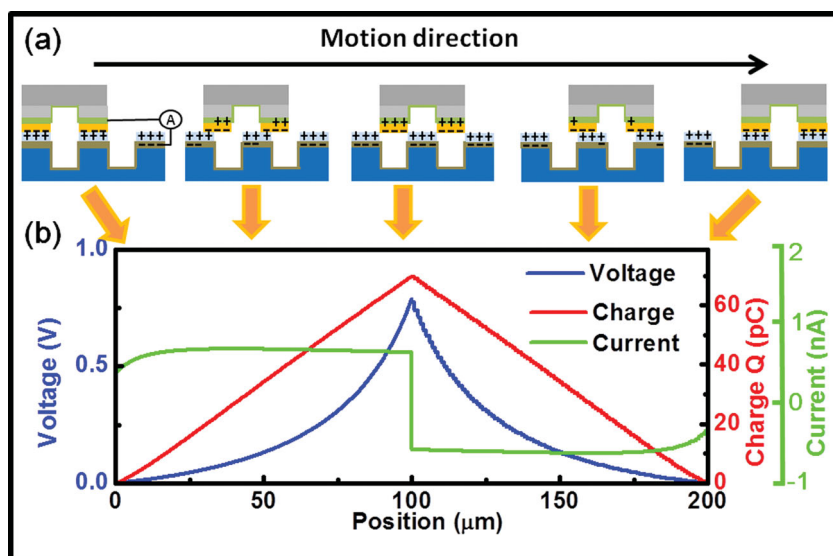

Figure 2. Working principle of the micrograting motion sensor. (a) Sketches that illustrate relative moving between the grating pair, leading to the charge transfer between two metal electrodes in SC condition. Within a cycle of the displacement, the micrograting pair experiences conditions of full overlap, partially separation, full separation, partially separation and full overlap. (b) Numerical simulation of the electrical potential in open circuit condition (blue curve) and charge in the top metal electrode in short circuit condition (red curve). Parameters used in simulation are described in Supporting Information. The short circuit current (green curve) is calculated from the charge change by assuming a constant moving speed of 1 mm s⁻¹. In OC condition, the potential valley and the peak present at two ends (full overlap) and the middle (full separate), respectively. In the SC condition, current changes signs from negative to positive at the two ends, from positive to negative in the middle.
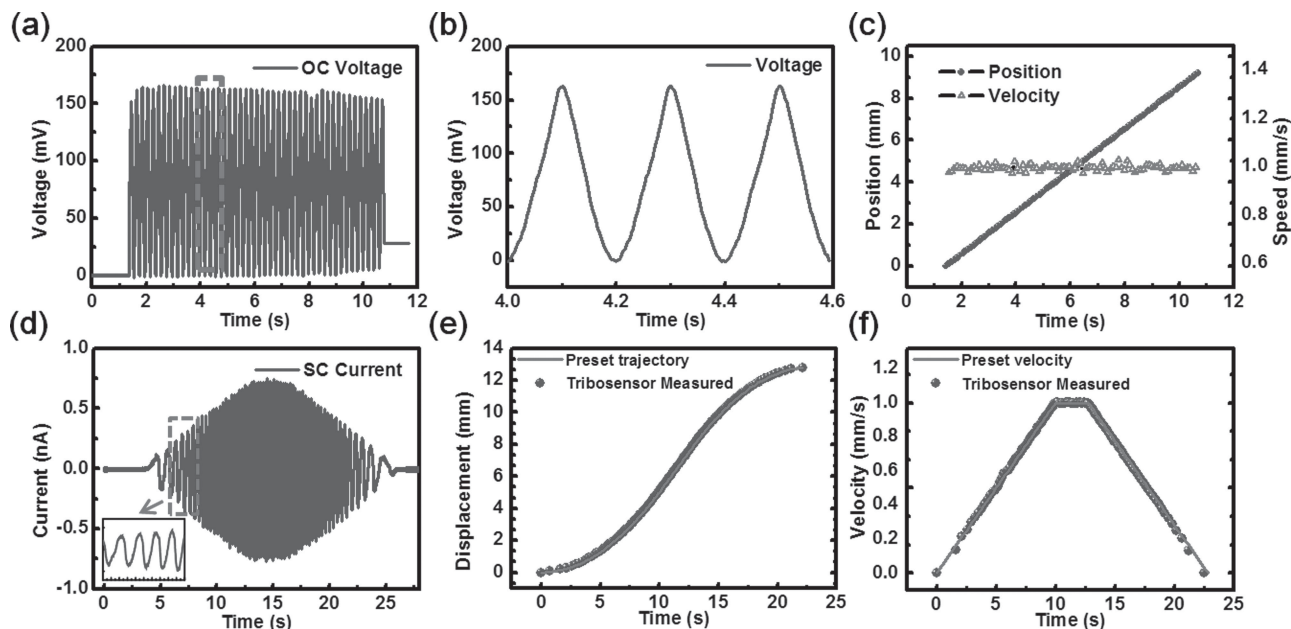
Figure 3. Demonstration of the long distance motion sensing by counting the OC voltage peak or SC current zero-crossings. (a) The OC voltage signals acquired from a displacement of 9.2 mm at a preset speed of 1 mm s^{-1}. (b) An enlarged view of the OC voltage signal from a, showing a similar shape as expected from aforementioned numerical simulation. (c) The real time displacement and speed derived from the measured voltage signal. (d) The SC current signals acquired from a non-uniform motion (decelerate – uniform speed – deceleration). (e) The preset motor's trajectory and the real time displacement detected by the motion sensor. (f) The preset motor's speed and the real time speed detected by the motion sensor.

displacement can be calculated by accumulating extra 200 μm once one more peak is detected. As shown in the blue curve in Figure 3c, the detected displacement increases linearly with time. With time frame simultaneously recorded, the real time motion speed can also be derived by dividing the width of one pitch (200 μm in this device) by the time interval between two adjacent voltage peaks, as shown in the red curve in Figure 2c. The average of the measured velocity is 0.994 ± 0.0^{-1}, which has 0.6% difference compared to the preset value. During a non-uniform motion testing, the motor was set to accelerate to 1 mm s^{-1} with a rate of 0.1 mm s^{-2}, maintain the speed and then decelerate at a rate of -0.1 mms^{-2} until stop. The SC current measured between the two electrodes is alternating between negative and positive periodically during the motion, as displayed in Figure 2d. By counting the number of zero-crossings, each of which counted as 100 μm step of displacement, the real time displacement can be derived and is shown

as the blue dots in Figure 2e. Compared with the preset trajectory as indicated in red curve, the measurement matched very well. Using a similar method for the speed calculation in uniform motion, a real time speed during this non-uniform motion can be obtained, as shown in Figure 2f. The advantage of the peak/zero-crossing counting method is that the measured displacement is independent of the magnitude (as long as it is above the noise level) of the output signal, suggesting its potential of direct interfacing with digital circuit after signal conditioning (e.g. pre-amplification), which would largely simplify the whole measurement system by avoiding complex analog to digital converting system.

Investigation on the voltage within a period can substantially enhance the resolution in displacement detection. Starting from a status with complete overlap, a step motion test with each step of 5 μm was performed. As shown in **Figure 4**a, the voltage at each position stays stable, benefited from the extreme
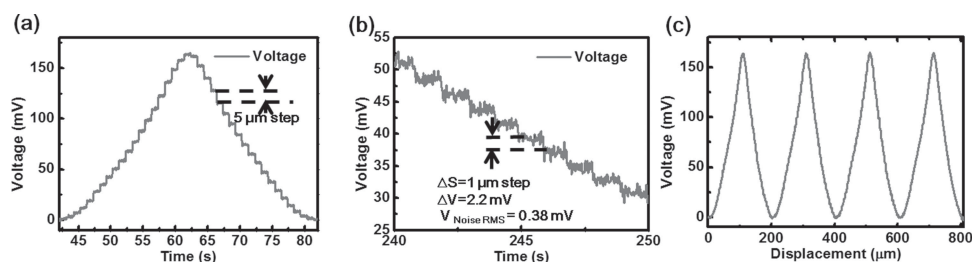

Figure 4. High resolution in displacement sensing realized by analyzing the magnitude of the OC voltage. (a) The OC voltage measured with a step motion of 5 μm per step within a pitch (200 μm). (b) Step motion with 1 μm per step in the sensitive region (10–190 μm) can be clearly resolved through the OC voltage signal. Given the RMS value of noise (0.38 mV), and the voltage change corresponding to 1 μm step motion (2.2 mV), the resolution can be calculated to be 173 nm. (c) OC voltage signal from 1 mm displacement. The shape of voltage signal within a pitch is very repeatable across pitches.

**ADVANCED
MATERIALS**

www.advmat.de

Materials
Views

www.MaterialsViews.com

COMMUNICATION

low mobility of the charges on the insulator surfaces.[20] The sensitive region is found to be from 10 μm to 190 μm, where each step motion of 1 μm can be clearly differentiated from the voltage response, as shown in Figure 2b. The change of the voltage for each step is about 2.2 mV, and the Root Mean Square (RMS) of the noise V_{noise} at 1 Hz is 0.38 mV (Supplementary Figure S3). Consequently, the displacement resolution at bandwidth of 1 Hz can be calculated to be 173 nm by

$$S = \frac{\Delta s}{\Delta V / V_{noise}^{RMS}} \tag{1}$$

where Δv is the change in output voltage in response to the displacement ?s. The voltage response within a pitch can be linearized by a pre-calibration through mathematically fitting the voltage-position curve. The as-fabricated sensor has a linearity error of less than 5% within the measured range of 100 μm. The shape of the voltage signal within a pitch is very repeatable across pitches, as shown in Figure 4c. Since this error is almost fixed within the full sensing range (25 mm in this device), the linearity error of this sensor is less than 0.02%.

In the applications when the real time speed is preferably to be directly detected without recording the time, it can be quantitatively correlated to the amplitude of the SC circuit current given small aspect ratio of the insulating layer (1:20 for Parylene and 1:200 for SiO_2 in this device) and thus negligible fringe effect on the electric field between two electrodes. As illustrated in Figure 2b, the amount of charges Q induced on the electrodes is approximately linearly correlated to the displacement,[21] as described by $Q = NW\sigma x$, where x is the relative displacement within a pitch, σ is the triboelectrically

transferred surface charge density on the top micro-grating, N and W are the total number of periods, and the width of the top grating, respectively. Therefore the current I, as a time derivative of charges Q, can be linearly correlated to the time derivative of the displacement—speed v, as indicated in Equation (2) and the green curve in Figure 2b.

$$I = \frac{dQ}{dt} = NW\sigma v \tag{2}$$

The experimental SC current output under a speed ranging from 10^{-5} m s^{-1} to 10^{-1} m s^{-1} is shown in **Figure 5**a-d with the scale of each chart an order magnitude larger than its previous one. The current in the four figures seems to have the "same" magnitude of their plateaus and valleys in their scales, indicating a very good linearity in sensing the speed over a 4 order of magnitude dynamic range. Figure 5e shows the plot of the magnitude of the detected current against motion speed from 5 μm s^{-1} to 10 mm s^{-1} and a linear fit that gives its sensitivity of (679 ± 4) pA/(mm s^{-1}) with adjusted R^2 = 0.99938. The resolution in dynamic speed detection is calculated to be 1.2 μm s^{-1} using similar approach as described in Equation (1), given the RMS value (0.8 pA) of the noise.

The resolution of the displacement and speed sensing can be further enhanced. For displacement sensing through OC voltage, with a linear approximation, the resolution (minimum detectable displacement) can be defined as the displacement range that corresponds to half of a cycle of the output signal (one cycle corresponds to one grating period P in this device) divided by the signal-noise ratio (SNR) of the output OC voltage. From a device perspective, on one hand, SNR can be enhanced
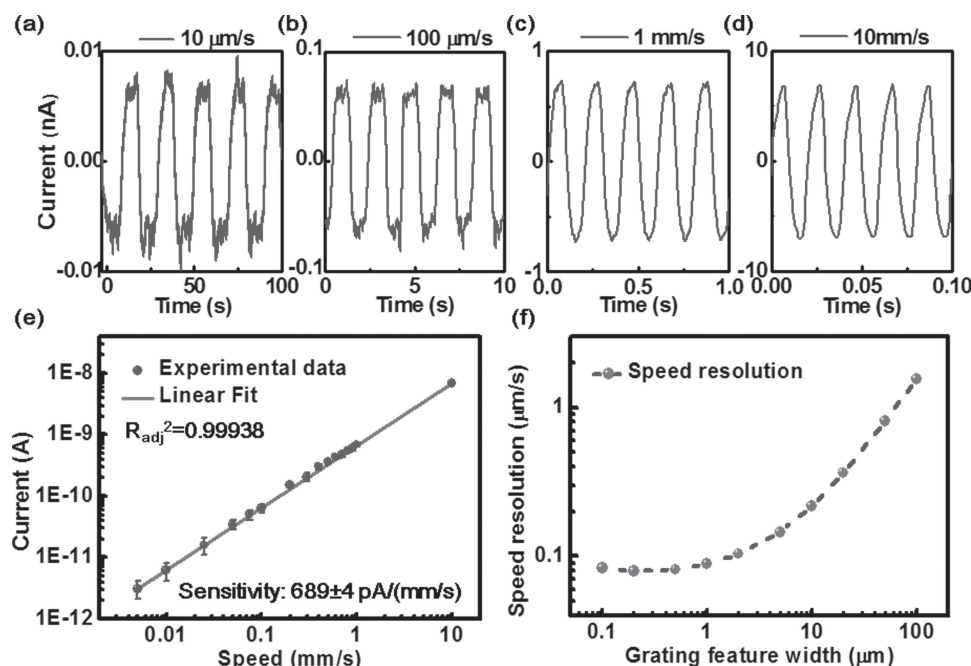

Figure 5. Dynamic speed detection *via* SC current. (a-d) The SC current measured with motion speed from 10 μm s^{-1}, 100 μm s^{-1}, 1 mm s^{-1}, 10 mm s^{-1}, respectively. (e) A plot of SC current as a function of motion speed from 5 μm s^{-1} to 10 mm s^{-1} with a fitted sensitivity of 689 ± 4 pA (mm s^{-1}). (f) Speed resolution for different grating feature width at the measurement noise level of 1 pA.

by increasing the amplitude of the sensor's OC voltage, which can be realized by increasing the triboelectric charge density at the interface through choosing more triboelectrically positive and negative materials as the triboelectric layers for the top and bottom grating, respectively.[16] On the other hand, the displacement range per cycle can be reduced by scaling down the grating's period (P). However, reducing the size of the grooves attenuates the OC voltage due to increased fringe effect of the electric field between two electrodes, as illustrated from the finite element simulation results shown in Figure S7. Therefore, there will be an optimized size of the grating so that relative decrease of the OC voltage is no larger than relative decrease of the grating size. We simulated the OC voltage in full separation condition using several different grating size, and find out the optimize size ($P/2$) would be around 20 μm with other structure parameters fixed.

Regarding dynamic speed sensing from SC current, according to Equation (2), the resolution can be further enhanced by increasing the number of gratings (N), the width of device (W), and/or the tribo-charge density σ using different triboelectric materials system. Provided fixed device area ($L{\times}W$), the number of gratings (N) can be increased by scale down the grating period (P) as $N = L/P$. Similarly, because of non-negligible fringe effect as grating size is shrunk down, the charges flowing between two metal electrodes during overlap-separation process are less than the triboelectric charges on the insulating surface. Therefore, there will also be a threshold grating width below which the current cannot be further enhanced. A finite element method is used to simulate this phenomenon, as discussed in details in Supporting Information. Considering the 1 pA (RMS value) of the measurement system noise level, the speed resolution can be optimized to be 107 nm s^{-1} using grating feature width of 2 μm (Figure S9).

Further enhancement of resolution can be realized by reducing the thickness of the dielectric (frictional) layers, which attenuates the fringe effect.

In summary, we have demonstrated a fundamentally new approach of employing triboelectric effect and electrostatic induction between a pair of microgratings for self-powered motion sensing. One dimensional displacement and speed can be detected using peak/zero-crossing counting method, which is very robust against variations caused by non-uniform surface charge distribution, surface contamination or grating defects. Analysis of the OC voltage amplitude improved the displacement resolution to be 173 nm for a grating width of 100 μm. The real time speed can be detected by the SC current amplitude, which shows a very good linear correlation with a large dynamic speed range from 5 μm s^{-1} to 0.1 m s^{-1}. Both displacement and speed resolution can be further improved but the limitation is also studied. Besides, the sensors can be easily scaled up with very low cost if laser interference lithography is used to fabricate the micro/nano gratings. This design opens a new paradigm for displacement/speed sensing by distinguishing itself from the existing technologies through a combination of self-powered, nano-resolution at a long working distance, high robustness and tolerance, non-optical simple structure as well as low cost. This technology has wide potential applications in automation, manufacturing, process control, etc.

Experimental Section

Fabricating the Micrograting Pair: For the top grating, a SU-8 layer with thickness of 17 μm was spin coated on a glass slide and patterned to be one dimensional grating (width: 100 μm, period: 200 μm) using photolithography. Afterwards, the grating was cut into desired size (15 mm × 30 mm for the presented device), followed by sputtering of Indium Tin Oxide (200 nm) and thermal coating of Parylene C (5 μm) using STS Parylene coater. For the bottom grating, a Si wafer was etched into periodical trenches (100 μm in width and 100 μm in depth) with 200 μm period using standard inductively coupled plasma (ICP) etching methods with patterned NR9–1500PY negative photoresist (from *Futurrex, Inc.*) as etching mask. Afterwards, a layer of Al (200 nm) was coated using DC sputter and SiO$_2$ (500 nm) deposited using plasma enhanced chemical vapor deposition (PECVD).

Displacement and Speed Measurement: The bottom grating was fixed on a platform, which was attached on a tilting stage that adjusts the alignment of the strips between the grating pair. The top grating was fixed to an Acrylic plate that is attached on a linear motorized stage (VP-25XA from *Newport Inc.*). Adhesive sponge (2 mm in thickness) was used to cushion the contact force for an intimate contact area between two grating planes. During the test, the linear motorized stage brought the top grating substrate to move in the direction perpendicular to the strips. The acceleration/deceleration rate was set to be ± 40 mm s^{-2} in the uniform velocity experiment (Figure 2a), and ± 0.1 mm s^{-2} in the non-uniform motion experiment (Figure 2d). The OC voltage and SC current was measured by an electrometer (6514 from Keithley Instruments), was measured by a current preamplifier (SR570 from Stanford Research System). A low pass filter (20 Hz) was used in data post-processing of OC voltage.

Supporting Information

Supporting Information is available from the Wiley Online Library or from the author.

Acknowledgements

[1] T. Yoshino, K. Kurosawa, K. Itoh, T. Ose, *Ieee J. Quantum. Elect.* **1982**, *18*, 1624.

[2] D. Rugar, H. J. Mamin, R. Erlandsson, J. E. Stern, B. D. Terris, *Rev. Sci. Instrum.* **1988**, *59*, 2337.

[3] P. C. F. Wolfenda, *J. Phys. E: Sci. Instrum.* **1968**, *1*, 817.

[4] P. B. Kosel, G. S. Munro, R. Vaughan, *Ieee T. Instrum. Meas.* **1981**, *30*, 114.

[5] H. Guckel, T. Earles, J. Klein, J. D. Zook, T. Ohnstein, *Sensor Actuat. A-Phys.* **1996**, *53*, 386.

[6] R. Knobel, A. N. Cleland, *Appl. Phys. Lett.* **2002**, *81*, 2258.

[7] Y. S. Zhou, R. Hinchet, Y. Yang, G. Ardila, R. Songmuang, F. Zhang, Y. Zhang, W. H. Han, K. Pradel, L. Montes, M. Mouis, Z. L. Wang, *Adv. Mater.* **2013**, *25*, 883.

[8] L. Persano, C. Dagdeviren, Y. W. Su, Y. H. Zhang, S. Girardo, D. Pisignano, Y. G. Huang, J. A. Rogers, *Nat. Commun* **2013**, 4.

COMMUNICATION

[9] R. G. Knobel, A. N. Cleland, *Nature* **2003**, *424*, 291.

[10] H. Klauk, U. Zschieschang, J. Pflaum, M. Halik, *Nature* **2007**, *445*, 745.

[11] S. Xu, Y. Qin, C. Xu, Y. G. Wei, R. S. Yang, Z. L. Wang, *Nat. Nanotechnol* **2010**, *5*, 366.

[12] R. L. Arechederra, S. D. Minteer, *Anal. Bioanal. Chem.* **2011**, *400*, 1605.

[13] Y. Yang, Y. S. Zhou, H. Zhang, Y. Liu, S. Lee, Z. L. Wang, *Adv. Mater.* **2013**, *256594*

[14] F. R. Fan, Z. T. Tian, Z. L. Wang, *Nano Energy* **2012**, *1*, 7.

[15] S. Wang, L. Lin, Y. Xie, Q. Jing, S. M. Niu, Z. L. Wang, *Nano Lett.* **2013**, *13*, 2226.

[16] G. Zhu, J. Chen, Y. Liu, P. Bai, Y. S. Zhou, Q. Jing, C. F. Pan, Z. L. Wang, *Nano Lett.* **2013**, *13*, 2282.

[17] F. R. Fan, L. Lin, G. Zhu, W. Z. Wu, R. Zhang, Z. L. Wang, *Nano Lett.* **2012**, *12*, 3109.

[18] Z. H. Lin, G. Zhu, Y. S. Zhou, Y. Yang, P. Bai, J. Chen, Z. L. Wang, *Angew. Chem. Int. Edit.* **2013**, *52*, 5065.

[19] L. Lin, S. H. Wang, Y. N. Xie, Q. S. Jing, S. M. Niu, Y. F. Hu, Z. L. Wang, *Nano Lett.* **2013**, *13*, 2916.

[20] Y. S. Zhou, Y. Liu, G. Zhu, Z. H. Lin, C. Pan, Q. Jing, Z. L. Wang, *Nano Lett.* **2013**, *13*, 6.

[21] S. Niu, Y. Liu, S. Wang, L. Lin, Y. S. Zhou, Y. Hu, Z. L. Wang, *Adv. Mater.* **2013**, *256184*